Boundary-Layer Meteorol (2008) 129:191–210
DOI 10.1007/s10546-008-9310-1

ORIGINAL PAPER

Microstructure of Turbulence in the Stably Stratified Boundary Layer

Zbigniew Sorbjan · Ben B. Balsley

Received: 5 April 2008 / Accepted: 25 August 2008 / Published online: 19 September 2008

Abstract The microstructure of a stably stratified boundary layer, with a significant low-level nocturnal jet, is investigated based on observations from the CASES-99 campaign in Kansas, U.S.A. The reported, high-resolution vertical profiles of the temperature, wind speed, wind direction, pressure, and the turbulent dissipation rate, were collected under nocturnal conditions on October 14, 1999, using the CIRES Tethered Lifting System. Two methods for evaluating instantaneous (1-sec) background profiles are applied to the raw data. The background potential temperature is calculated using the "bubble sort" algorithm to produce a monotonically increasing potential temperature with increasing height. Other scalar quantities are smoothed using a running vertical average. The behaviour of background flow, buoyant overturns, turbulent fluctuations, and their respective histograms are presented. Ratios of the considered length scales and the Ozmidov scale are nearly constant with height, a fact that can be applied in practice for estimating instantaneous profiles of the dissipation rate.

Keywords Boundary-layer measurements · Boundary-layer turbulence · Ozmidov scale · Stable boundary layer · Tethered lifting system · Thorpe scale

1 Introduction

According to conventional wisdom, stably stratified and horizontally homogeneous turbulence can be characterized by background (filtered) state parameters. The development of small-scale turbulence is assumed to result from the competition between the background wind shear, associated primarily with the streamwise velocity, and the stabilizing effects of the background buoyancy. The wind shear S supplies the kinetic energy for turbulent motion, while buoyancy, expressed by the Brunt-Väisälä frequency $N = ((g/T_o)d\Theta/dz)^{1/2}$, acts

Z. Sorbjan (✉)
Department of Physics, Marquette University, Milwaukee, WI 53201-1881, USA
e-mail: sorbjanz@mu.edu

B. B. Balsley
Cooperative Institute for Research in Environmental Sciences,
University of Colorado, Boulder, CO, USA

to restrain it (here, Θ is the background virtual potential temperature, g is the buoyancy acceleration, and T_o is the reference virtual temperature). If $S^2 > N^2$, shear production dominates, and turbulence is amplified. On the other hand, if $S^2 < N^2$, buoyancy prevails and turbulence is suppressed, and eventually decays. Linear stability theory implies that small turbulent perturbations grow exponentially when the Richardson number of the background flow, $Ri = N^2/S^2$, is limited by a critical value $Ri_{cr} = 1/4$ everywhere in the fluid (e.g., Miles 1961; Howard 1961; Woods 1969).

It is becoming increasingly clear, however, that such a classical concept of stable turbulence regimes is not sufficient. First of all, the conventional approach does not include the effects of buoyancy waves. Processes associated with the intermittent breaking of internal waves constitute a major source of turbulence (Fritts and Rastogi 1985). Blumen (2001) reported the occurrence of billows approximately 300 m in length, contained in a layer depth of 30 m, and translated over the observational site for approximately 30 min. Fritts et al. (2003) documented a ducted-wave event with an apparent horizontal wavelength of a few kilometres, and a wave phase speed slightly larger than the mean wind in the direction of propagation.

Turbulent flows in the stable boundary layer (SBL) contain thin, quasi-horizontal layers that have large, positive and negative vertical gradients (e.g., Balsley et al. 1998; 2003). Continuous high-resolution echoes in the stable boundary layer provided by radar and sodar sounders indicate that such layering systems are randomly distributed, a few metres deep, many kilometres long, and modulated by internal buoyancy waves on multitude scales (Chimonas 1999). During the passage of internal buoyancy waves, these thin layers and steep gradient regions can move up and down by many tens of metres.

There is a rising body of observational evidence suggesting that turbulence survives at Richardson numbers exceeding unity (e.g., Galperin et al. 2007). The Richardson number is not a unique characteristic of the flow, and strongly depends on the definition of the basic state and the vertical resolution of measurements. It can strongly fluctuate with height around the critical value, causing its interpretation to be sometimes vague (e.g., De Silva et al. 1999).

Observations, especially those obtained during the Cooperative Atmosphere–Surface Exchange Study-1999, CASES-99 (e.g., Banta et al. 2002; Poulos et al. 2002; Balsley et al. 2003), show that an ample understanding of the stably stratified boundary layer depends on high-resolution vertical measurements. Similarly, large-eddy simulations indicate that an accurate description of the SBL requires about 1-m spatial resolution (e.g., Beare and MacVean 2004). Therefore, it is not so obvious that an adequate description of the extremely complex structure of turbulence in the stable regime can be retrieved from filtered state parameters, as implied by the conventional approach, or obtained based on vertically coarse measurements.

The goal of this paper is to address the above issues by analyzing the microstructure of the stably stratified boundary layer. For this purpose high-resolution profiles, collected by the Tethered Lifting System (TLS) during the CASES-99 experiment, will be considered. The paper has the following structure: first, the TLS system is briefly reviewed in Sect. 2. Section 3 presents an analysis of the instantaneous (1-sec) background flow, buoyant overturns, turbulent fluctuations, and their histograms and relevant scales. Final remarks are presented in Sect. 4.

2 TLS Description

The Tethered Lifting System (hereafter, TLS) was developed by the Cooperative Institute for Research in Environmental Sciences (CIRES) at the University of Colorado in Boulder,

U.S.A. The system employs either a high-tech kite, or an aerodynamic balloon, to lift a series of turbulence packages, suspended at prescribed intervals below the lifting platform (Balsley 2008). During the CASES-99 experiment, which took place in Kansas in the autumn of 1999, the TLS instrumentation included both a basic meteorological payload and a series of turbulence payloads.

The basic meteorological payload archived 1-sec reference values of temperature, pressure, humidity, wind speed and direction, telemetry, and various "housekeeping" details. Each of the turbulence packages collected high-frequency (200-Hz) fluctuations of both temperature and wind speed, using cold-wire and hot-wire sensors, respectively. The turbulence payloads also carried conventional low-frequency sensors, i.e., a Pitot tube, a solid-state temperature sensor, and a piezo-electric pressure sensor for sampling mean wind speed, temperature, and pressure, along with a three-axis tilt sensor and a magnetic compass for wind direction measurements. Separate archiving for each payload package was accomplished by using onboard digital flash-memory storage.

All TLS results were essentially point-source measurements, although in the profiling mode the vertical resolution of 1-s samples was on average 0.34 m (standard deviation equal to 0.15 m). The vertical velocity of the sensor packages, for both ascents and descents, was approximately $0.4\,\mathrm{m\,s^{-1}}$, so that a single profile required somewhat more than 15 min. Determinations of the dissipation rate ε and the temperature structure constant C_T^2 were made during post-analysis, using techniques described by Frehlich et al. (2003).

There are a number of inherent advantages and disadvantages associated with the TLS technique. Advantages include very high vertical resolution, continuous altitude coverage from the surface to 1–2 km, and the ability to launch a series of instrumented packages suspended at intervals from the same tether. This final feature enables a determination of vertical gradients over a few metres and provides an easy method of inter-calibration between packages. A listing of specific disadvantages includes the difficulty of accurately determining the vertical velocity and vertical fluxes, and the inability to operate in inclement weather or in clouds.

3 Results

3.1 Raw Profiles

Over 60 vertical TLS profiles were collected during CASES-99. In this paper, we consider only two profiles, obtained on the night of October 14, 1999 (IOP 6). The first profile was made beginning at 0745 UTC (0145 LST), while the second profile began four hours later, at 1148 UTC (0548 LST), about 1 h before sunrise. Three other TLS profiles, separated by 1 h intervals, are also available for the period under study, but are not presented in this paper. Furthermore, although data from two additional payload packages were recorded during the flights under study, our analysis is limited only to data from one package.

The boundary layer on the night of October 14 1999 evolved under a light surface wind (about $1\,\mathrm{m\,s^{-1}}$) and clear sky conditions (e.g., Fritts et al. 2003; Balsley 2006). Near-surface temperatures decreased steadily from 7.5°C at the beginning of the observation period to 4°C prior to local sunrise. Raw vertical profiles of the pertinent flights are presented in Fig. 1.

This depicts 1-sec profiles of potential temperature, wind velocity, wind direction, and the energy dissipation rate. Note that all of the profiles displayed in the figure exhibit significant small-scale fluctuations with height. As we will show in subsequent sections, these fluctuations are real and strongly inter-related.

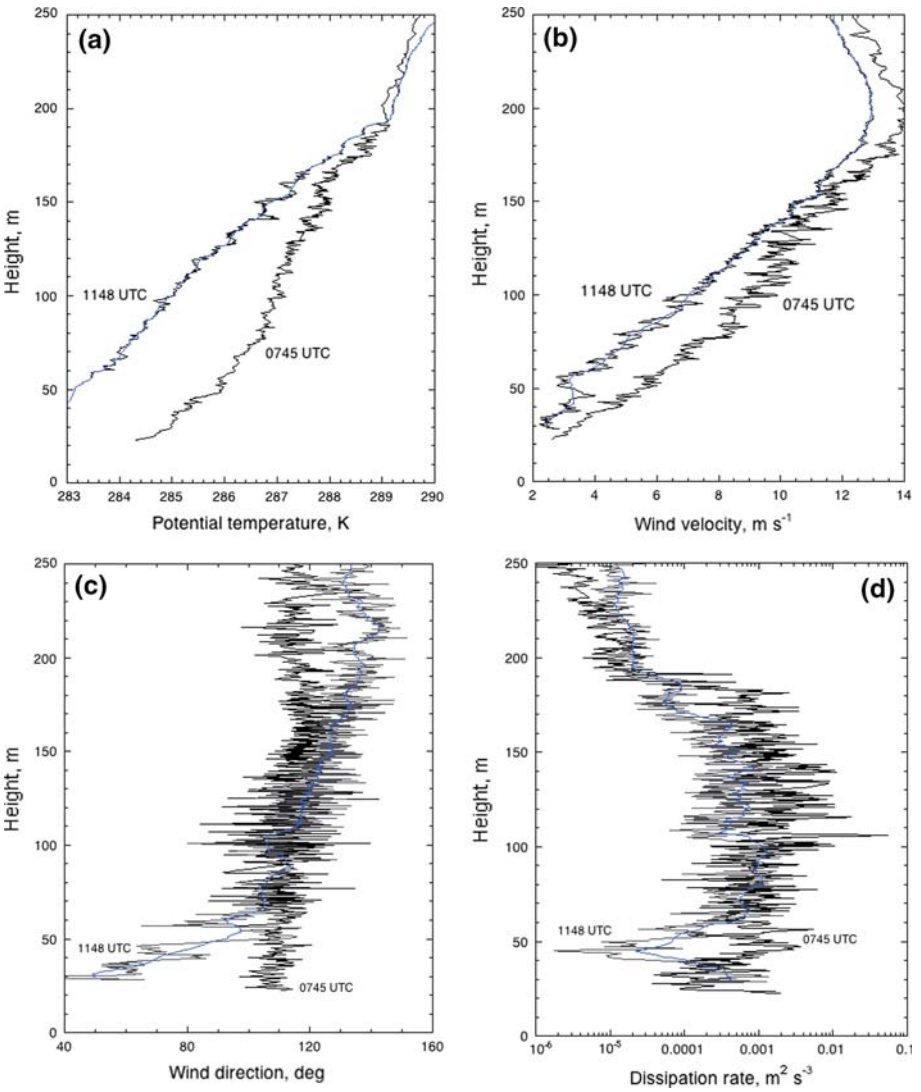

Fig. 1 Profiles of: (**a**) potential temperature, (**b**) wind velocity, (**c**) wind direction, and (**d**) dissipation rate, obtained during CASES-99 at 0745 UTC, and at 1148 UTC of October 14, 1999. The background profiles (blue lines) are plotted only for profiles at 1148 UTC

Examination of Fig. 1a shows that the temperature at about 25 m above the surface decreases gradually at a rate of about $0.6\,\mathrm{K\,h^{-1}}$ in the interval from 0745 to 1148 UTC. The potential temperature profile at 0745 UTC appears to have a three-layer structure, with different vertical gradients. The potential temperature below the 100-m level reveals a positive curvature, with a mean gradient of about $36\,\mathrm{K\,km^{-1}}$; between 100 and 190 m, the profile exhibits a negative curvature with a mean gradient of about $19\,\mathrm{K\,km^{-1}}$, and finally, the gradient above 190 m is about $3\,\mathrm{K\,km^{-1}}$. This three-layer structure is also apparent at 1148 UTC, although it is less pronounced.

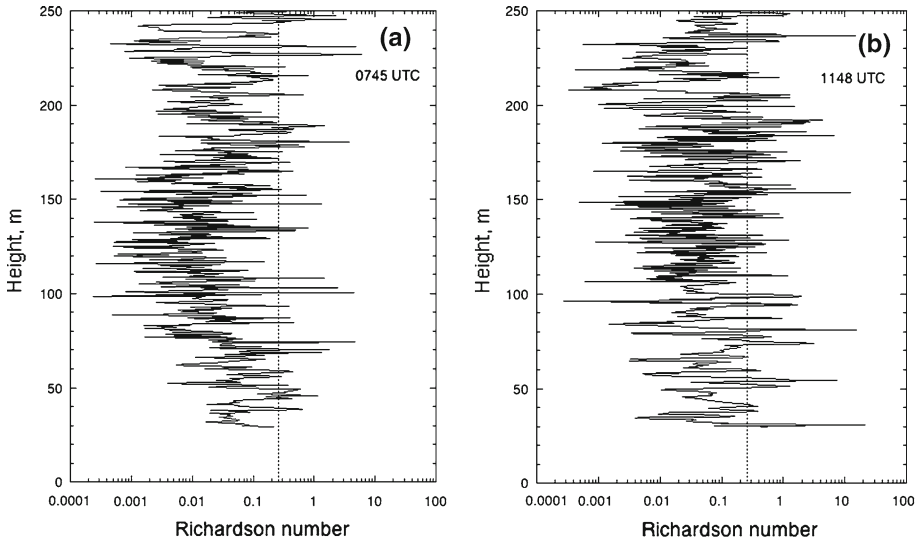

Fig. 2 Profiles of the Richardson number at: (**a**) 0745 UTC, and (**b**) 1148 UTC. The critical value Ri_c is marked by a dotted line

The sudden fall in the temperature gradient at about 190 m marks the top of the boundary layer. Another estimate of the stable boundary-layer height h can be obtained based on the critical value of the Richardson number in the form:

$$h = \sqrt{Ri_c}\frac{U_m}{\overline{N}} \tag{1}$$

where U_m is the maximum wind velocity in the stable boundary layer, and $\overline{N}$ is the mean Brunt-Väisälä frequency. For $U_m = 14\,\mathrm{m\,s^{-1}}$, $\overline{N} = 0.038\,\mathrm{s^{-1}}$, and $\sqrt{Ri_c} = 0.5$, we obtain $h = 184\,\mathrm{m}$.

The layer above 190 m is only slightly transformed by radiative cooling (see e.g., Fritts et al. 2003, Fig. 2), and it can be identified as the residual layer, a remnant of the previous day's mixed layer, with its own dynamic activity observed throughout the nighttime (Mahrt and Vickers 2006; Balsley 2008). Vertical velocities in this layer, recorded by the University of Wyoming King-Air B200 research aircraft, are presented by Nappo (2002, Fig. 1.3), and show wave-like structures, identified as ducted buoyancy waves (Nappo 2003; Fritts et al. 2003). Banta et al. (2002) present the horizontal variability of the wind on that night, as seen in profiler/sodar data.

The wind velocity profile in Fig. 1b shows a low-level jet at the height of 190 m, with a maximum velocity of about $14\,\mathrm{m\,s^{-1}}$ at 0745 UTC, and $13\,\mathrm{m\,s^{-1}}$ at 1148 UTC. The mean wind shear below 190 m, is about $7\,\mathrm{m\,s^{-1}\,km^{-1}}$ in both profiles. The wind direction at 0745 UTC, in Fig. 1c, changes only slightly with height, from about 110° near the surface to about 120° at 300 m. At 1148 UTC, however, the wind direction varies from about 90° at 50 m to about 135° at 300 m. This notable clockwise shift, to a more southerly flow in the upper layers on the latter profile, is most likely due to the effects of inertial oscillations.

The fluctuations of the dissipation rate ε in Fig. 1d are real and substantial (note that a logarithmic horizontal scale is used in the figure). Within the 50–175 m layer at 0745 UTC, the dissipation rate is in the range of 10^{-3}–$10^{-2}\,\mathrm{m^2\,s^{-3}}$, and these values decrease by roughly

an order of magnitude at 1148 UTC, particularly at higher heights. A significant decrease of the dissipation rate above 190 m is comparable, but discernable in the two profiles.

3.2 Background Profiles

An adequate knowledge of turbulence requires specification of the background environment. This is not an easy task, particularly when observations consist of single, instantaneous profiles. To facilitate appropriate understanding under these limitations, we have applied two separate methods for evaluating background profiles. The first method pertains only to the potential temperature profiles, while the second method is employed for all of the other scalar quantities. This procedure is justified by the requirement that the background virtual potential temperature profile must be a monotonically increasing function of height under stable conditions. With this stipulation the Brunt–Väisälä frequency N remains a real function of height. Note that we have ignored the effect of humidity in this study, for the sake of simplicity, and have based our calculations on the potential temperature, even though employing the virtual potential temperature would generally be more appropriate.

The background potential temperature is calculated here following the method proposed by Thorpe (1977), which involves the reordering of a non-monotonic profile of the potential temperature Θ(z) into a monotonic profile defined here as $\tilde{\Theta}(z)$. This is accomplished by an evaluation of "overturns" in the potential temperature profiles. The overturns are defined as occurring at those levels where the potential temperature profile decreases with increasing height. Following this procedure, the resulting $\tilde{\Theta}(z)$ profile is an approximation to the profile that would be measured if the turbulence were allowed to relax adiabatically to a motionless state. This concept has been previously used in the analysis of oceanic, lake, and laboratory measurements, as well as in numerical experiments, applied to the analysis of strong mixing events near the tropopause (e.g., Winters et al. 1995; Caulfield and Peltier 2000; Smyth and Moum 2000; Luce et al. 2002; Gavrilov et al. 2005).

The re-ordering procedure above can be explained by considering a discrete vertical profile of the potential temperature $\{\Theta_1, \ldots, \Theta_N\}$, defined at levels z_j, where $j = 1, 2, \ldots, n$. The method applies a "bubble sort" algorithm, which generates the potential temperature sequence in monotonically increasing order $\{\Theta_{i1} \leq \Theta_{i1} \ldots \leq \Theta_{iN}\}$, where $\{i_1, \ldots, i_n\}$ is a permutation of a sequence $\{1, \ldots, n\}$. The algorithm progresses in steps numbered j, where $j = n, \ldots, 1$. For each j, the values $\Theta(z_k)$, where $k = 1, \ldots, j-1$, are analyzed, beginning at the lowest height. An interchange, or "swapping" of the temperature values of the adjacent levels, is performed when $\Theta(z_k) > \Theta(z_{k+1})$. As a result of this procedure, the highest temperature is moved to the top of each overturning region. This process is repeated for a temperature sequence decreased by one. The resulting monotonically reordered profile at 1148 UTC is shown in Fig. 1a.

If air at any level z_j is moved to the level z_k to generate a stable, monotonic potential temperature profile, it is possible to define the Thorpe displacement as:

$$\Delta Z_j = z_j - z_k. \tag{2}$$

The value of ΔZ_j describes the depth of a density overturn in the stable stratified fluid. Note that strong mixing is characterized by large displacements, which are negative at the top and positive at the bottom of each overturning event. There is an obvious conceptual analogy between the values of these displacements and the mixing length used in early turbulence theories.

As mentioned above, for scalars other than potential temperature, we apply only a 25-point running average:

$$\overline{U}_j = \frac{1}{25} \sum_{k=-12}^{12} U_{j+k} \tag{3}$$

where U can be the wind velocity modulus, wind velocity components, wind direction, or the dissipation rate. These smoothed 25-point averaged profiles for wind velocity, wind direction, and the dissipation rate for 1148 UTC, are plotted as the thick lines in Fig. 1b–d.

The 25-point running average is equivalent to a low-pass filter. Its width is on average equal to 8.6 m, owing to the approximate TLS ascent/descent rate of 0.4 m s^{-1}. The standard deviation of this quantity is 3.1 m, due to fact that the vertical velocity of the TLS changed with height. Specifically, the filter width is about 10 m near the surface, about 5 m at 150 m, and about 12 m at 250 m. We have determined that this variation has a relatively minor effect on the filtered values, and also found that $\overline{\Theta} \neq \tilde{Q}$, i.e. that the 25-point smoothed potential temperature profiles differ from those produced by sorting, and are not monotonic.

3.3 Richardson Number and Surface Heat Flux

The gradient Richardson number is evaluated using the monotonic potential profile $\tilde{\Theta}(z)$ as:

$$Ri_j = \frac{N_j^2}{S_j^2} \tag{4}$$

where S_j is the wind shear, and N_j is the Brunt-Väisälä frequency at level j:

$$N_j^2 = \frac{g}{T_o}\left(\frac{d\tilde{\Theta}}{dz}\right)_j = \frac{g}{T_o}\frac{\tilde{\Theta}_{j+1} - \tilde{\Theta}_{j-1}}{z_{j+1} - z_{j-1}}, \tag{5a}$$

$$S_j^2 = \left(\frac{d\overline{U}}{dz}\right)_j^2 + \left(\frac{d\overline{V}}{dz}\right)_j^2 = \left[\frac{\overline{U}_{j+1} - \overline{U}_{j-1}}{z_{j+1} - z_{j-1}}\right]^2 + \left[\frac{\overline{V}_{j+1} - \overline{V}_{j-1}}{z_{j+1} - z_{j-1}}\right]^2, \tag{5b}$$

and $\overline{U}$ and $\overline{V}$ are vertically-averaged components of the wind velocity.

The resulting gradient Richardson numbers are shown in Fig. 2a and b for the two profiles under study. Fluctuations in the figures are substantial (note the logarithmic horizontal scale), and the presence of adjacent layers can be noticed, with values of Ri significantly above and below the critical value Ri_c. This fact implies that the concept of the local gradient Richardson number is ambiguous in cases characterized by non-linear background parameters.

Comparison of Fig. 2a and b suggests that the smaller Ri values at 0745 UTC should correspond to generally more intense turbulence during that period, relative to the latter case. On average, Ri is 0.11 up to 190 m above the Earth's surface at 0745 UTC, with minimum and maximum values lying between 0.0002 and 4.6 (on average $N^2 \approx 0.001\,\mathrm{s}^{-2}$, and $S^2 \approx 0.09\,\mathrm{s}^{-2}$). Above the 190 m level, Richardson numbers exhibit wavy, quasi-periodic undulations with height. On average at 1148 UTC, Ri is 0.27 in the 190-m layer above the Earth's surface, with minimum and maximum values in the range from 0.0003 to 21 ($N^2 \approx 0.001\,\mathrm{s}^{-2}$, $S^2 \approx 0.06\,\mathrm{s}^{-2}$). Since the values of Ri are shifted toward larger values, the situation at 1148 UTC is thus expected to be less turbulent.

Note that the cooling rate at the level of 190 m in Fig. 1a is about zero. Using the background temperature equation, assuming that the heat flux at the top of the SBL vanishes,

and also that the contribution of the radiative flux within the SBL can be neglected, we obtain:

$$\hat{H}(z_L) = \frac{1}{(t_2 - t_1)} \int_{z_L}^{h} \left[\tilde{\Theta}(z, t_2) - \tilde{\Theta}(z, t_1) \right] dz \tag{6}$$

where $\hat{H}$ is the average turbulent heat flux in the interval (t_1, t_2), h is the depth of the boundary layer, t_1 and t_2 are instants of time, and z_L is the height near the underlying surface. Based on Fig. 1, we obtain $\hat{H} \approx -0.006\,\mathrm{K\,m\,s^{-1}}$ at $z_L = 30\,\mathrm{m}$. The mean values of the heat flux (over a much shorter time interval), evaluated by Balsley (2006,Fig. 11); using 55-m tower data, are lower.

3.4 Scalar Fluctuations

We define the potential temperature fluctuations as:

$$\Theta'_j = \Theta_j - \tilde{\Theta}_j, \tag{7}$$

with negative fluctuations Θ'_j are associated with negative displacements ΔZ_j. The fluctuations for other scalars we will be defined as:

$$U'_j = U_j - \overline{U}_j \tag{8}$$

where U is the wind velocity, wind direction, or the dissipation rate.

Based on (2) (3), (7), and (8), we also specify the following statistical measures of the magnitude of each varying quantity:

$$\delta Z_j = \overline{|\Delta Z_j|}, \tag{9a}$$

$$\delta \Theta_j = \overline{|\Theta'_j|}, \tag{9b}$$

$$\delta U_j = \overline{|U''_j|}, \tag{9c}$$

$$\sigma_{Zj} = \left[\overline{(\Delta Z_j)^2} \right]^{1/2}, \tag{9d}$$

$$\sigma_{\Theta j} = \left[\overline{(\Theta'_j)^2} \right]^{1/2}, \tag{9e}$$

$$\sigma_{Uj} = \left[\overline{(U''_j)^2} \right]^{1/2}, \tag{9f}$$

which will be employed in Sect. 3.6. Note, that the absolute measures in (9) are equivalent to the standard deviations. We verified that the absolute means are smaller than the quadratic means, e.g., $\delta Z_j = 0.74 \sigma_{Zj}$ (standard deviation = 0.11 m).

The vertical distributions of displacements ΔZ_j are depicted in Fig. 3a, b. Figure 3a refers to the profile at 0745 UTC, and shows several, relatively deep overturning events, with centres at levels of 80, 120, 150, 180, and 200 m. The displacements in the largest event, around the level of 150 m, are in the range from about −20 to 20 m. The overturning events above 200 m are intermittent with height, and relatively small, and as indicated in Fig. 3b, the overturning

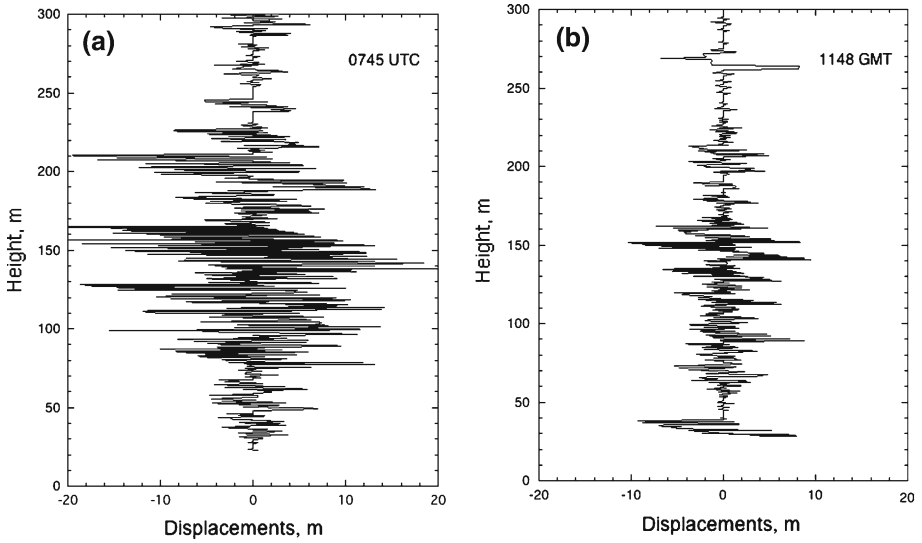

Fig. 3 Profiles of displacement ΔZ_j calculated from Eq. 2 at: (**a**) 0745 UTC, and (**b**) 1148 UTC

activity diminishes with time, as more stable stratification gradually develops. The largest displacements, at 1148 UTC, range from about −10 to 10 m at the level of 150 m.

The vertical distributions of the temperature fluctuations Θ'_j are depicted in Fig. 4a, b. The overturning events are less clearly marked compared to those in Fig. 3. The temperature fluctuations at 0745 UTC increase with height, and are the largest in the layer from about 140 to 190 m. The amplitude of oscillations in this layer is about 0.4 K, and the temperature fluctuations decrease with time. The temperature fluctuations at 1148 UTC increase with height, and are the largest in the layer from about 130 to 160 m.

The wind velocity fluctuations U''_j (not shown) do not seem to be correlated with the displacements ΔZ_j, nor the temperature fluctuations Θ'_j. At 0745 UTC, they increase with height, and are the largest in the layer from about 100 to 150 m, where they range from about -0.8 to 1 m s^{-1}. The fluctuations U''_j decrease with time; at 1148 UTC, they are the largest in the lowest layer, up to the level of about 100 m, where they range from about −0.5 and 0.5 m s^{-1}.

The vertical distributions of the wind direction fluctuations α''_j (not shown) are nearly uniform with height. The largest excursions occur at 0745 UTC, and are located in the layer from about 80 to 130 m, where they range from approximately −20° to 20°. The fluctuations only slightly change with time. The largest fluctuations at 1148 UTC are located in the layer from about 100 to 130 m, where they range between −12° and 12°.

3.5 Histograms

Our analysis can further be refined by analysis of histograms, obtained for displacements and fluctuations. In Fig. 5, histograms for the vertical displacements ΔZ_j are displayed; other histograms, which are not shown, look similar, and therefore are only characterized by their statistics in Table 1.

The distributions in Fig. 5 seem to be made of two exponential functions. This is not surprising, since exponential distributions are known to occur naturally in cases describing

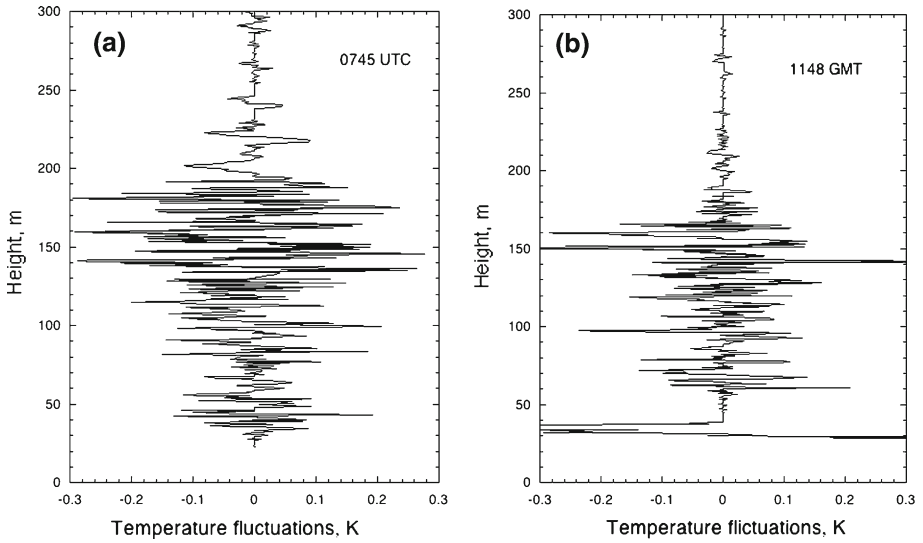

Fig. 4 Profiles of the temperature fluctuations Θ'_j calculated from Eq. 7 at: (**a**) 0745 UTC, and (**b**) 1148 UTC

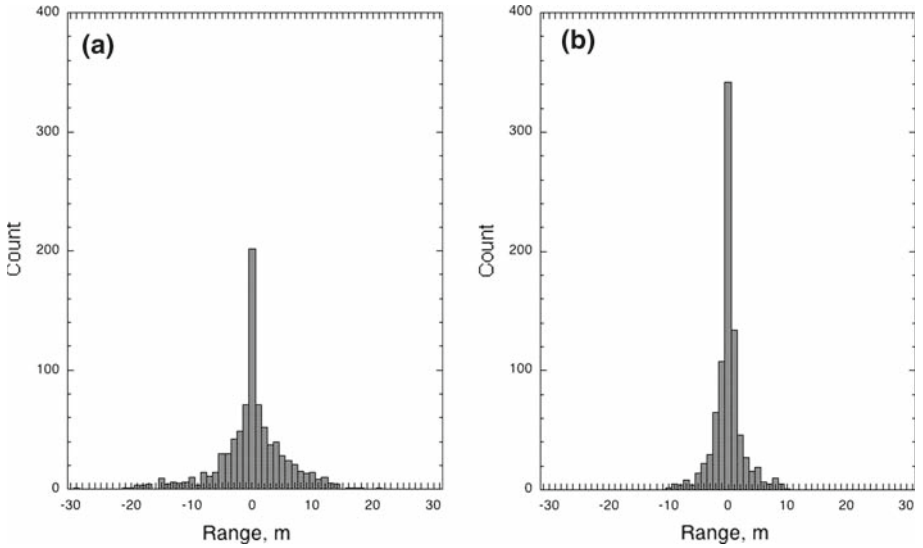

Fig. 5 Histograms of the displacements ΔZ_j at: (**a**) 0745 UTC, and (**b**) 1148 UTC

the number of "events" per unit time or distance, which occur in homogeneous Poisson processes. The difference between two independent, identically distributed, exponential random variables, is governed by a double exponential distribution, also refered to as the Laplace distribution (Abramowitz and Stegun 1972). The distribution can be thought of as two exponential distributions, joined together back-to-back.

When the mean value is zero, as in our case, the double exponential distribution is described by the density function of the form $f(x) = \frac{1}{2s} e^{-|x|/s}$, and standard deviation σ equal to $\sqrt{2}s$.

Table 1 Statistical characteristics of considered histograms

	Standard deviation	Skewness	Kurtosis
0745 UTC			
Δz_j, m	5.678	−0.535	5.432
Θ'_j, K	0.079	−0.051	4.750
U''_j, m s^{-1}	0.256	0.223	5.310
α''_j, deg	6.900	0.123	4.887
1148 UTC			
Δz_j, m	2.540	0.087	6.373
Θ'_j, K	0.081	−0.241	11.970
U''_j, m s^{-1}	0.168	0.011	6.860
α''_j, deg	6.925	−0.282	5.110

Since the density function is symmetric, the skewness $S = \mu_3/\sigma^3 = 0$, where μ_3 is the third moment about the mean, and due to the heavier tails, kurtosis $K = \mu_4/\sigma^4 = 6$, where μ_4 is the fourth moment about the mean. Kurtosis can be considered as an indicator of the degree of intermittency, with larger values indicative of processes with greater intermittency (e.g., Blumen 2001). Higher kurtosis means that more of the variance is due to infrequent extreme deviations. For comparison, kurtosis for the normal distribution is equal to 3.

The statistical characteristics of the considered histograms are shown in Table 1, which indicates that the standard deviations decrease with time, for displacements and wind velocity, and are nearly the same for temperature and wind direction. The values of kurtosis at 0745 UTC are about 5, and at 1148 UTC, kurtosis is larger than 6 for all variables, except for wind direction, for which it is equal to about 5. The skewness is not zero, as would be expected, and can be explained by the fact that all statistical moments can be easily distorted by extreme values in the tails. The frequencies at the origin of the histograms at 1148 UTC are larger, except for wind direction.

3.6 Relevant Scales

Stably stratified turbulent flows are governed by the relative strength of local buoyancy, shear, and viscous forces. Their effects can be quantified using length scales, obtained from dimensional analysis and physical arguments. The result, however, is not unique to stable conditions, since various scaling sets can be formed in this case (Sorb 2008a, b). This fact differentiates stable flows from convective or neutral turbulence, which is usually characterized by single length scales (e.g., Fernando and Hunt 1996).

According to Kolmogorov's theory (1943), the smallest eddies in the SBL are isotropic, and at the size of the Kolmogorov length scale:

$$L_k = \frac{\nu^{3/4}}{\varepsilon^{1/4}} \tag{10}$$

where ν is the molecular viscosity, and ε is the dissipation rate. Larger eddies must overcome the effects of the buoyancy force in order to become isotropic, and this can take place only for eddies formed by substantial velocity gradients. The theory of locally isotropic turbulence indicates that the change of velocity ΔU over a distance L is: $\Delta U \sim \varepsilon^{1/3} L^{1/3}$. Thus, the mean velocity gradient can be expressed as: $dU/dL \sim \varepsilon^{1/3}/L^{2/3}$. In order to evaluate the size of turbulent eddies, for which the effects of the buoyant forces are overpowered by wind shear, an analogue of the Richardson number can be defined, and assumed equal to its critical value:

$$Ri = \frac{N^2}{(\varepsilon^{1/3} L^{-2/3})^2} = Ri_c \tag{11}$$

where N is the Brunt–Väisälä frequency. From this, the length scale, often referred to as the Ozmidov scale, can be obtained in the form (e.g., Ozmidov 1968):

$$L_o = \frac{\varepsilon^{1/2}}{N^{3/2}}, \tag{12}$$

where dimensional analysis implies that the equivalent velocity scale is $V_o = \varepsilon^{1/2}/N^{1/2}$, and the temperature scale $T_o = \varepsilon^{1/2} N^{1/2}/\beta$.

The Ozmidov scale L_o defines the size of the largest isotropic eddies that are able to exist despite buoyancy. In flows where turbulence and wave motion are simultaneously present, the inverse of the Ozmidov scale defines the buoyancy wavenumber that separates the buoyancy from the inertial subrange. The Froude number, $Fr = \varepsilon/(\nu N^2)$, proportional to the ratio of L_o and L_k, characterizes the separation of scales between the largest scale of turbulence not controlled by buoyancy, and the smallest viscous scales. As stable turbulence decays, L_o decreases. Ultimately, all scales of turbulence are actively inhibited by buoyancy, and the Froude number decreases.

An equivalent length scale can be obtained by expressing the dissipation rate in (12) as $\varepsilon \sim \sigma_w^3/L$, where σ_w^2 is the vertical velocity variance. This yields:

$$L_w = \frac{\sigma_w}{N}, \tag{13}$$

and the resulting scale can be seen as indicative of the greatest distance a fluid particle can move against the density gradient. The equivalent velocity scale is $V_w = \sigma_w$, and the temperature scale $T_w = \sigma_w N/\beta$ (Sorbjan 2006).

Another scale can be derived by equating the production and dissipation terms in the temperature variance equation, leading to:

$$L_\theta = \frac{\beta \sigma_\theta}{N^2}, \tag{14}$$

which scale is an estimate of vertical excursions in a stratified fluid against buoyancy stratification (Ellison 1957). It can also be derived by assuming that the temperature fluctuation $\theta' = l' N^2/\beta$, where l' is the vertical displacement, for which $\sqrt{\overline{l'^2}} = L_\theta$. The equivalent velocity scale is $V_\theta(z) = \beta \sigma_\theta/N$, and the temperature scale $T_\theta(z) = \sigma_\theta$ (Sorbjan 2006, Sorbjan 2008a,b).

Sorbjan (2008a) concluded from two composite cases described by Mahrt and Vickers (2006) that the scaling (14) yields more consistent results than that based on (13). The dimensionless moments, scaled by (14), approach constant values for sufficiently large values of the dimensionless height of Ri. Itsweire et al. (1993) showed direct numerical simulation of homogeneous turbulence that when $Ri < Ri_c$, both L_o and L_θ grow slightly with time, when the flow is fully developed. When $Ri > Ri_c$, the range of overturning turbulent scales decreases until $L_o \approx 9 L_K$. When $Ri = Ri_c$, all three length scales L_o, L_θ and L_k may eventually reach a constant with time.

Monin and Obukhov (1954) introduced a scale that indicates the size of eddies for which the local production of turbulence by stress $\tau^{3/2}/L_*$ is balanced by the energy loss through work against the buoyancy βH:

$$L_* = \frac{\tau^{3/2}}{\kappa \beta H} \tag{15}$$

where τ, H, are the turbulent fluxes of momentum and temperature, and κ is von Karman constant. The equivalent velocity scale in this case is $U_* = \tau^{1/2}$, and the temperature scale $T_* = -H/U_*$. Sorbjan (2006) argued that the "flux-based" scaling (15) is valid only in cases of strong, continuous turbulence, when the gradient Richardson number Ri is constant and sub-critical. For weak turbulence (very stable regime), the "gradient-based" scaling based on (12)–(14) is more appropriate.

Thorpe (1977) proposed a scale directly related to density overturns from instantaneous temperature profiles. The scale can be defined as the root-mean-square of the vertical displacements ΔZ in (2) required to reorder a measured profile to be gravitationally stable:

$$L_Z = \left\langle \Delta Z^2 \right\rangle^{1/2} \tag{16}$$

where $\langle\rangle$ indicates the average over a single overturn. Because overturns are one-dimensional, the scale gives a good estimate of an overturn size, as long as the flow is horizontally homogeneous. Based on the previously applied expression for the temperature fluctuation $\theta' = l' N^2/\beta$, it follows that $L_Z = \sqrt{\overline{\Delta Z^2}} \sim \sqrt{\overline{l'^2}} = L_\theta$. Moreover, it can be expected that the product $L_Z^2 N^2$ is a measure of the vertical velocity variance of the overturns, while the product $L_Z^2 N^3/\beta$ is proportional to the turbulent heat flux.

It can be anticipated that if $L_T << L_o$, turbulence is fully developed, nearly isotopic, and independent of buoyancy forces. When $L_T \approx L_o$, vertical overturning becomes inhibited by buoyancy, and anisotropic turbulence starts to develop. Various measurements in oceans and lakes have shown, however, that the Thorpe scale is usually nearly equal to the Ozmidov scale. Based on maritime observations, Dillon (1982) found that $L_T \approx 1.25 L_o$, and Crawford (1986) obtained a larger coefficient $L_T \approx 1.52 L_o$ for the oceanic thermocline, while Ferron et al. (1998) received $L_T \approx 1.05 L_o$ for an abyssal region.

3.7 Scale Evaluation

The scales mentioned above can be evaluated locally, or as averages over the entire, or part of the, domain. Herein we choose to define the scales based on the 25-point running average (3), employing the quantities listed in (5) and (9). Specifically, the Ozmidov length, and the related velocity and temperature scales, are evaluated as:

$$L_{oj} = \frac{\left(\overline{\varepsilon_j}\right)^{1/2}}{\left(\overline{N_j^2}\right)^{3/4}}, \tag{17a}$$

$$V_{oj} = \frac{\left(\overline{\varepsilon_j}\right)^{1/2}}{\left(\overline{N_j^2}\right)^{1/4}}, \tag{17b}$$

$$T_{oj} = \frac{\left(\overline{\varepsilon_j}\right)^{1/2} \left(\overline{N_j^2}\right)^{1/4}}{\beta}, \tag{17c}$$

where the subscript j indicates that the scales are calculated at each level z_j.

The scales defined in (17) are presented in Fig. 6. At 0745 UTC, all scales exhibit strong fluctuations with height, and seem to reflect the overturning events displayed in Fig. 3a. On average, the Ozmidov scale L_o is about 10 m in the 190-m layer, with values in the range from 2 to 40 m. The scale decreases with time, due to the development of more stable stratification, and at 1148 UTC, its vertical distribution is more uniform. On average, L_o is about

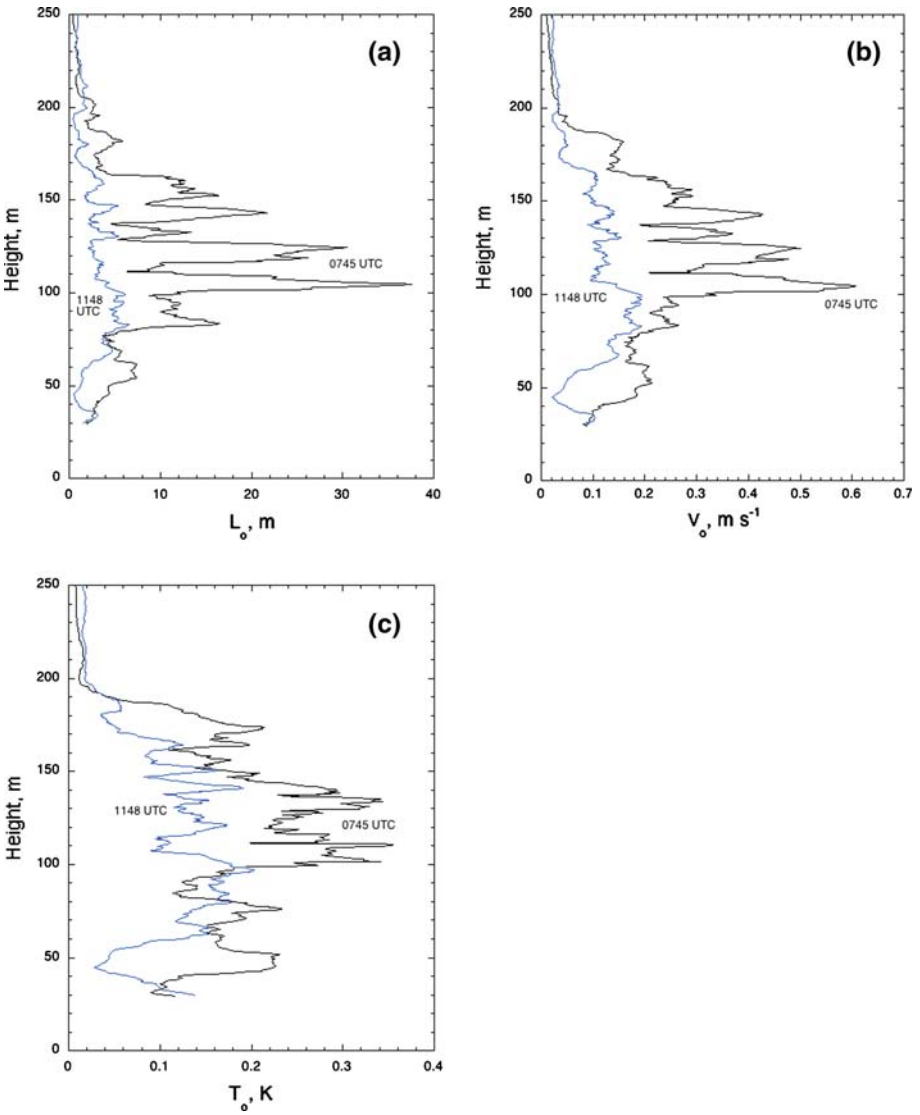

Fig. 6 Profiles of: (**a**) Ozmidov length scale L_{oj}, (**b**) velocity scale V_{oj}, and (**c**) temperature scale T_{oj}, at 0745 UTC (black lines), and at 1148 UTC (blue lines)

2.8 m in the 190-m layer, with values in the range from 0.5 to 6.5. The velocity scale V_o has a very similar distribution, and also reflects the overturning events displayed in Fig. 3a. At 0745 UTC, on average, V_o is 0.25 m s^{-1}, and at 1148, has decreased to 0.10 m s^{-1}. The temperature scale T_o at 0745 UTC is on, average, equal to 0.2 K in the 190-m layer, and at 1148 UTC has reduced to 0.12 K.

The scale (14) and the related scales are evaluated as:

$$L_{\theta j} = \frac{\beta \delta \Theta_j}{\overline{N_j^2}}, \tag{18a}$$

Table 2 The estimates of all considered scales in the 190 m-layer

UTC	L_{oj},m	V_{oj}, m s^{-1}	T_{oj}, K	$L_{\theta j}$, m s^{-1}	$V_{\theta j}$, m s^{-1}	$T_{\theta j}$, K	L_{Zj}, m	V_{Zj}, m s^{-1}	T_{Zj}, K
0745	10.0	0.25	0.20	3.8	0.1	0.07	5.9	0.16	0.09
1148	2.8	0.10	0,12	1.3	0.05	0.06	2.3	0.07	0.07

$$V_{\theta j} = \frac{\beta \delta \Theta_j}{\left(\overline{N_j^2}\right)^{1/2}}, \tag{18b}$$

$$T_{\theta j} = \delta \Theta_j. \tag{18c}$$

Note that σ_{Θ_j} can also be used in (18) instead of $\delta\Theta_j$, which is not expected to significantly change the above scales.

The scales (18) strongly fluctuate with height (not shown). At 0745 UTC, on average, the scale $L_{\theta j}$ is 3.8 m in the 190-m layer, with values in the range from 0.2 to 12.5, and decreases with time, due to the development of a more stable stratification. At 1148 UTC, its vertical distribution is more uniform, and on average, $L_{\theta j}$ is 1.3 m in the 190-m layer, with values in the range from 0.01 to 6. The velocity scale $V_{\theta j}$ has a very similar distribution. At 0745 UTC, on average $V_{\theta j}$ is about 0.1 m s^{-1}, and at 1148, has decreased to 0.05 m s^{-1}. The temperature scale $T_{\theta j}$ is on average equal to 0.07 K at 0745 UTC, and at 1148 UTC its average value in the 190-m layer is 0.06 K.

We now introduce the analogue of the Thorpe scale, and equivalent velocity and temperature scales, in the form:

$$L_{Zj} = \sigma_{Zj}, \tag{19a}$$

$$V_{Zj} = \left(\beta \sigma_{Z\,j} \sigma_{\Theta\,j}\right)^{1/2}, \tag{19b}$$

$$T_{Zj} = \sigma_{\Theta\,j}. \tag{19c}$$

The profiles of these scales look very similar to the profiles of those from (17). They strongly fluctuate with height (not shown) and decrease with time due to the development of a more stable stratification. At 0745 UTC, L_{Zj} is on average equal to 5.9 m (the standard deviation is 2.7 m) in the 190-m-layer, while at 1148 UTC, L_{Zj} is 2.3 m (standard deviation = 1.3 m, large values below 40 m were excluded). The decrease of L_{Zj} in time implies that turbulence acquires an anisotropic structure due to suppressed vertical mixing.

The velocity scale V_{Zj} at 0745 UTC is on average equal to 0.16 m s^{-1} (the standard deviation is 0.06 m s^{-1}) in the 190-m layer, and at 1148 UTC, its average value has decreased to 0.07 m s^{-1} (standard deviation = 0.04 m s^{-1}). The temperature scale T_{Zj} at 0745 UTC is on average equal to 0.09 K (the standard deviation is 0.03 K), and at 1148 UTC, has decreased to 0.07 K (the standard deviation is 0.04 K). The above estimates are summarized in Table 2.

3.8 Scale Dependencies

A comparison of the Ozmidov scale and related scales (16), with the scales listed in (18), is shown in Fig. 7, indicating that within the SBL:

$$\frac{L_{Zj}}{L_{oj}} \approx 0.6, \tag{20a}$$

$$\frac{V_{Zj}}{V_{oj}} \approx 0.5, \tag{20b}$$

$$\frac{T_{Zj}}{T_{oj}} \approx 0.4, \tag{20c}$$

for both cases (large values near the surface were not included). The fact that the above ratios are approximately constant (in the considered range of *Ri)* can be applied in practice to reconstruct instantaneous profiles of the dissipation rate based on high-resolution measurements of temperature.

A comparison of the velocity scale V_{oj}, defined in (17b), with the parameter δU_j listed in (9) is shown in Fig. 8, showing that approximately:

$$\frac{\delta U_j}{V_{oj}} \approx 1 \tag{21}$$

(large values near the surface were not included). From (21) it follows that in the specified range of height, the instantaneous profiles of the dissipation can also be approximately reconstructed based on wind fluctuations.

We also verified that within the boundary layer, approximately:

$$\frac{\delta Z_j}{L_{oj}} \approx 0.4, \tag{22a}$$

$$\frac{\delta \Theta_j}{T_{oj}} \approx 0.4. \tag{22b}$$

The obtained relationships (20)–(22) imply an existence of a general similarity regime, for which a statistical moment X can be expressed as: $\frac{X_j}{L_{oj}^a V_{oj}^b T_{oj}^c} = const$. Remarkably, the similarity seems to be valid for instantaneous parameters.

Applying the definitions (17) and (18), one can also obtain:

$$\frac{L_{\theta j}}{L_{oj}} = \frac{V_{\theta j}}{V_{oj}} = \frac{T_{\theta j}}{T_{oj}} = r, \tag{23}$$

which, together with (20)–(22), indicate that the scales (17), (18) and (19) are equivalent (since they are proportional). We confirmed that the parameter r is nearly constant with time, independent of height, and on average equal to about 0.4 within the SBL.

From (17)–(18) and (22)–(23), we have that, approximately:

$$\left(\overline{\frac{d\tilde{\Theta}}{dz}}\right)_j = \frac{T_{\Theta_j}}{L_{\Theta j}} = \frac{T_{oj}}{L_{oj}} \approx \frac{\delta \Theta_j}{\delta Z_j} \tag{24}$$

and since $\left(\overline{d\tilde{\Theta}/dz}\right)_j$ increases in time, the ratio $T_{\theta j}/L_{\theta j}$ must also increase, mostly due to the decreasing values of $L_{\theta j}$.

4 Conclusions

Microstructure of the stably stratified boundary layer has been investigated, based on high-resolution atmospheric observations made during CASES-99 on October 14, 1999. Two

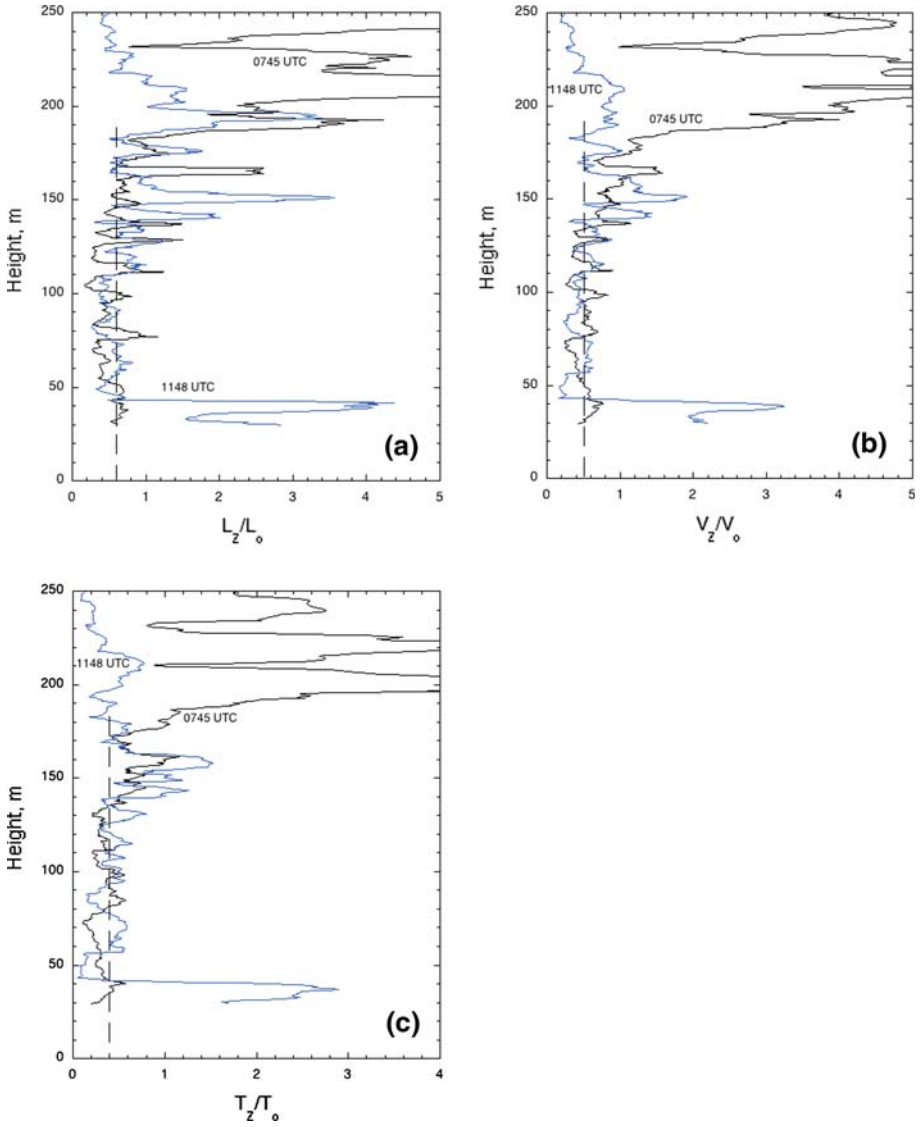

Fig. 7 Profiles of: (**a**) length scale ratio L_{Zj}/L_{oj}, (**b**) velocity scale ratio V_{Zj}/V_{oj}, and (**c**) temperature scale ratio T_{Zj}/T_{oj}, at 0745 UTC (black lines), and at 1148 UTC (blue lines)

instantaneous soundings, reported in this paper, were collected using the CIRES Tethered Lifting System. The first sounding was performed at 0745 UTC, while the second was at 1148 UTC, about 1 h before sunrise.

Two methods for evaluating background profiles have been applied to the raw data. The background potential temperature has been calculated and based on the one-dimensional sorting algorithm. For other scalars (wind velocity, direction, and dissipation rate), the vertical running average, defined over 25 adjacent points, has been applied. The vertical displacements

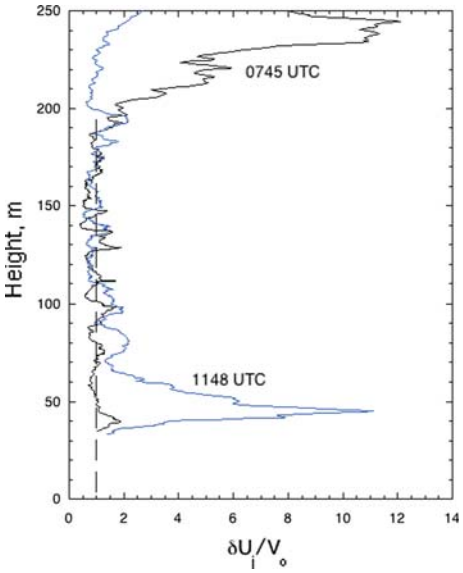

Fig. 8 Profiles of the ratio $\delta U_j / V_{oj}$ at: 0745 UTC (black line), and 1148 UTC (blue line)

ΔZ_j, and fluctuations Θ'_j, U''_j, α''_j, around the background parameters, have been calculated and analyzed.

The vertical displacements ΔZ_j mark several, relatively deep overturning events in the SBL. The overturning activity diminishes with time, as greater stable stratification develops. The overturning events above the SBL are intermittent and relatively small.

The histograms of displacements ΔZ_j and the fluctuations Θ'_j, U''_j, α''_j indicate that all variables are governed by double exponential distributions. The values of kurtosis at 0745 UTC are about 5, and at 1148 UTC, kurtosis is larger than 6 for all variables, except for the wind direction, for which it is equal to about 5. The skewness is not zero, and was most likely distorted by extreme values in the tails.

The height of the boundary layer has been estimated at about 190 m, for both cases, and a substantial scatter characterizes the profiles of the Richardson number. The presence of adjacent layers is observed, with the values of *Ri* significantly above and below the critical value. The case at 0745 UTC is found to be more turbulent, as there exists only a relatively small number of layers with overcritical values of *Ri* in the SBL. On average, the Richardson number *Ri* equals 0.11 at 0745 UTC, and 0.27 at 1148 UTC. Above the level of 190 m, the Richardson numbers undergoes wavy undulations along the z-axis.

Several scales for length, temperature, and velocity in the SBL have been considered and evaluated: (i) the Ozmidov length scale L_{oj}, and related scales based on the dissipation rate, (ii) the scale $L_{\theta j}$ and related scales based the temperature fluctuations, and finally, (iii) the scale L_{Zj} and related scales based the vertical displacements. The considered scales have been shown to be equivalent. The results implied an existence of a general similarity regime, for which statistical moments can be expressed in terms of the scales L_o, V_o, and T_o. Remarkably, the similarity seems to be valid for instantaneous parameters.

The estimates of the scales and their ratios provide relevant information for large-eddy simulations of nocturnal turbulence, and can also be applied in practice to estimate the dissipation rate, based on high-resolution measurements of temperature and wind velocity.

References

Abramowitz M, Stegun IA (eds) (1972) Handbook of mathematical functions: with formulas, graphs, and mathematical tables. Dover, New York, 1044 pp

Balsley BB (2008) The CIRES tethered lifting system: a survey of the system, past results and future capabilities. Acta Geophys 5:21–57. doi:10.2478/s11600-007-0045-z

Balsley BB, Jensen ML, Frehlich R (1998) The use of state-of-the-art kites for profiling the lower atmosphere. Boundary-Layer Meteorol 87:1–25. doi:10.1023/A:1000812511429

Balsley BB, Frehlich RG, Jensen ML, Meillier Y, Muschinski A (2003) Extreme gradients in the nocturnal boundary layer: structure, evolution and potential causes. J Atmos Sci 60:2496–2508. doi:10.1175/1520-0469(2003)060<2496:EGITNB>2.0.CO;2

Balsley BB, Frehlich RG, Jensen ML, Meillier Y (2006) High-resolution in situ profiling through the stable boundary layer: examination of the SBL top in terms of minimum shear, maximum stratification, and turbulence decrease. J Atmos Sci 63:1291–1307. doi:10.1175/JAS3671.1

Balsley BB, Svensson G, Tjernström M (2008) On the scale-dependence of the gradient Richardson number in the residual layer. Boundary-Layer Meteorol 127:57–72. doi:10.1007/s10546-007-9251-0

Banta RM, Newsom RK, Lundquist JK, Pichugina YL, Coulter RL, Mahrt L (2002) Nocturnal low-level jet characteristics over Kansas during cases-99. Boundary-Layer Meteorol 105:221–252. doi:10.1023/A:1019992330866

Beare RJ, MacVean MK (2004) Resolution sensitivity and scaling of large-eddy simulations of the stable boundary layer. Boundary-Layer Meteorol 112:257–281. doi:10.1023/B:BOUN.0000027910.57913.4d

Blumen W, Robert Banta R, Burns SP, Fritts DC, Newsome R, Poulos GS, Sun J (2001) Turbulence statistics of a Kelvin–Helmholtz billow event observed in the night-time boundary layer during the cooperative atmosphere–surface exchange study field program. Dyn Atmos & Oceans 34:189–204. doi:10.1016/S0377-0265(01)00067-7

Caulfield CP, Peltier WR (2000) The anatomy of the mixing transition in homogeneous and stratified free shear layers. J Fluid Mech 413:1–47. doi:10.1017/S0022112000008284

Chimonas H (1999) Steps, waves and turbulence in the stably stratified planetary boundary layer. Boundary-Layer Meteorol 90:397–421. doi:10.1023/A:1001709029773

Crawford WR (1986) A comparison of length scales and decay times of turbulence in stably stratified flows. J Phys Oceanogr 26:1847–1854. doi:10.1175/1520-0485(1986)016<1847:ACOLSA>2.0.CO;2

De Silva IP, Brandt D, Montenegro ALJ, Fernando HJS (1999) Gradient Richardson number measurements in a stratified shear layer. Dyn Atmos & Oceans 30:47–63. doi:10.1016/S0377-0265(99)00015-9

Dillon TM (1982) Vertical overturns: a comparison of Thorpe and Ozmidov length scales. J Geophys Res 87:9601–9613. doi:10.1029/JC087iC12p09601

Ellison TH (1957) Turbulent transport of heat and momentum from an infinite rough plane. J Fluid Mech 2:456–466. doi:10.1017/S0022112057000269

Fritts DC, Rastogi PK (1985) Convective and dynamical instabilities due to buoyancy wave motions in the lower and middle atmosphere: theory and observations. Radio Sci 20:1247–1277. doi:10.1029/RS020i006p01247

Fritts DC, Nappo C, Riggin CM, Balsley BB, Eichinger WE, Newsom RK (2003) Analysis of ducted motions in the stable nocturnal boundary layer during CASES-99. J Atmos Sci 60:2450–2472. doi:10.1175/1520-0469(2003)060<2450:AODMIT>2.0.CO;2

Fernando HJS, Hunt JC, (1996) Some aspects of turbulence and mixing in stably stratified layers. Dyn Atmos & Oceans 23:35–62. doi:10.1016/0377-0265(95)00422-X

Ferron B, Mercier H, Speer K, Gargett A, Polzin K (1998) Mixing in the Romanche fracture zone. J Phys Oceanogr 28:1929–1945. doi:10.1175/1520-0485(1998)028<1929:MITRFZ>2.0.CO;2

Frehlich RY, Meillier M, Jensen L, Balsley BB (2003) Turbulence measurements with the CIRES tethered lifting system during CASES-99: calibration and spectral analysis of temperature and velocity. J Atmos Sci 60:2487–2495. doi:10.1175/1520-0469(2003)060<2487:TMWTCT>2.0.CO;2

Galperin B, Sukoriansky S, Anderson PS (2007) On the critical Richardson number in stably stratified turbulence. Atmos Sci Lett 8:65–69. doi:10.1002/asl.153

Gavrilov NM, Luce H, Crochet M, Dalaudier F, Fukao S (2005) Turbulence parameter estimations from high-resolution balloon temperature measurements of the MUSTI-2000 campaign. Ann Geophys 23:2401–2413

Howard LN (1961) Note on a paper of John W. Miles. J Fluid Mech 10:509–512. doi:10.1017/S0022112061000317

Itsweire EC, Koseff JR, Briggs DA, Ferziger JH (1993) Turbulent in stratified shear flows: implications for interpreting shear-induced mixing in the ocean. J Phys Oceanogr 28:1508–1522. doi:10.1175/1520-0485(1993)023<1508:TISSFI>2.0.CO;2

Luce H, Fukao S, Dalaudier F, Crochet M (2002) Strong mixing events observed near the tropopause with the MU radar and high-resolution balloon techniques. J Atmos Sci 59:2885–2896. doi:10.1175/1520-0469(2002)059<2885:SMEONT>2.0.CO;2

Mahrt L, Vickers D, (2006) Extremely weak mixing in stable conditions. Boundary-Layer Meteorol 119:19–39. doi:10.1007/s10546-005-9017-5

Miles JW (1961) On the stability of heterogeneous shear flows. J Fluid Mech 10:496–508. doi:10.1017/S0022112061000305

Monin AS, Obukhov AM (1954) Basic laws of turbulence mixing in the surface layer of the atmosphere. Trudy Geof Inst AN SSSR 24:163–187

Nappo CJ (2002) An introduction to atmospheric buoyancy waves. Academic Press, 279 pp

Nappo CJ (2003) Observations of buoyancy wave modulated turbulence in the stable boundary layer during CASES-99 field study. Geophys Res Abstr 5:01786

Ozmidov PB (1968) Horizontal turbulence and turbulent exchange in the ocean. Publishing House “Science”, Moskow, 212 pp

Poulos GS, Blumen W, Fritts DC, Lundquist JK, Sun J, Burns SP, Nappo C, Banta R, Newsome R, Cuxart RJ, Terradwllas E, Basley BB, Jensen M (2002) Cases-99: a comprehensive investigation of the stable nocturnal boundary layer. Bull Am Meteorol Soc 4:576–581

Smyth WD, Moum JN (2000) Length scales of turbulence in stably stratified mixing layers. Phys Fluids 12:1343–1362. doi:10.1063/1.870386

Sorbjan Z (2006) Local structure of turbulence in stably stratified boundary layers. J Atmos Sci 63:1526–1537. doi:10.1175/JAS3704.1

Sorbjan Z (2008a) Local scales of turbulence in the stable boundary layer. Boundary-Layer Meteorol 127:1573–1472. doi:10.1007/s10546-007-9260-z

Sorbjan Z (2008b) Gradient-based similarity in the atmospheric boundary layer. Acta Geophys 5:220–233

Thorpe SA (1977) Turbulence and mixing in a Scottish loch. Philos Trans R Soc Lond A 286:125–181. doi:10.1098/rsta.1977.0112

Winters K, Lombard P, Riley J, D’Asaro EA (1995) Available potential energy and mixing in density-stratified fluids. J Fluid Mech 289:115–128. doi:10.1017/S002211209500125X

Woods JD (1968) Wave-induced shear instability in the summer thermocline. J Fluid Mech 32:791–800. doi:10.1017/S0022112068001035